Scalable Synthetic Approach to Inexpensive Methanol-Tolerant ORR Electrocatalysts Using Microporous Polymer Composite

Abin Sebastian[1], Atanu Panda[1], Ravi Nandan[1], Joel Henzie[1], Ovidiu Cretu[2], Jian Xu[3], Nadiia Velychkivska[1], Renzhi Ma[1], Pooja Gakhad[4], Abhishek Kumar Singh[4], Gary J. Richards[5], Koji Kimoto[2], Lok K. Shrestha[1,6], Katsuhiko Ariga[1,7], Yusuke Yamauchi[8,9,10], and Jonathan P. Hill*[,1]

[1]Research Center for Materials Nanoarchitectonics (MANA), National Institute for Materials Science (NIMS), Tsukuba 305-0044, Ibaraki, Japan

[2]Center for Basic Research on Materials (CFRM), National Institute for Materials Science (NIMS), Tsukuba 305-0044, Ibaraki, Japan

[3]International Center for Young Scientists (ICYS), National Institute for Materials Science (NIMS), Tsukuba 305-0044, Ibaraki, Japan

[4]Materials Research Centre, Indian Institute of Science, Mathikere, Bengaluru, Karnataka 560012, India

[5]Department of Applied Chemistry, Graduate School of Engineering and Science, Shibaura Institute of Technology, Fukasaku 307, Minuma-ku, Saitama-shi, Saitama 337-8570, Japan

[6]Department of Materials Science, Faculty of Pure and Applied Sciences, University of Tsukuba 1-1-1, Tennodai, Tsukuba 305-8573, Ibaraki, Japan

[7]Department of Advanced Materials Science, Graduate School of Frontier Sciences, The University of Tokyo, 5-1-5 Kashiwanoha, Kashiwa, Chiba 277-8561, Japan

[8]Department of Materials Process Engineering, Graduate School of Engineering, Nagoya University, Nagoya 464−8603, Japan

[9]Department of Chemical and Biomolecular Engineering, Yonsei University, 50 Yonsei-ro, Seodaemun-gu, Seoul 03722, South Korea

[10]Australian Institute for Bioengineering and Nanotechnology (AIBN) and School of Chemical Engineering, The University of Queensland, Brisbane, Queensland 4072, Australia

Email: Jonathan.Hill@nims.go.jp

TOC Graphic

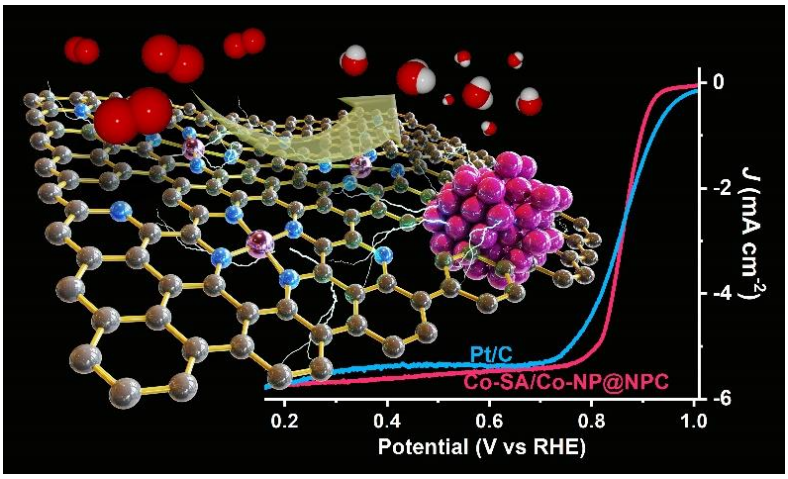

Abstract

The oxygen reduction reaction (ORR) is vital for renewable energy conversion and storage technology and requires effective electrocatalysts for its operation. Platinum-containing amorphous carbon-based materials are the current benchmark industrial catalysts for ORR so that the development of noble-metal-free electrocatalyst alternatives would be advantageous for the wider application of these technologies. Here, we report an efficient ORR electrocatalyst containing cobalt single atom and cobalt nanoparticle active sites embedded in a porous nitrogen-doped graphitic carbon network whose synthesis involves controlled thermolysis of metallated microporous porphyrin polymers. The properties of the resulting material relies on the coexistence of cobalt nanoparticles and cobalt single atom catalysts in an N-doped carbon matrix presenting a graphitic carbon protective layer, which acts as a prophylactic against oxidation of the Co-containing catalytically active sites. The robust electrocatalyst exhibits superior electrochemical ORR activity with onset and halfwave potentials of 0.96 V and 0.87 V (vs RHE), respectively. The electrocatalyst also shows excellent durability and methanol tolerance compared to the commercial benchmark Pt/C catalyst further enhancing the potential of this system for practical applications. Computational methods were used to assess the roles of the material components.

Keywords: Oxygen reduction reaction electrocatalyst, microporous porphyrin polymer, cobalt nanoparticle, cobalt single-atom catalyst.

Introduction

The increasing global demand for energy resources, coupled with escalating environmental challenges, has stimulated an intensive research effort in the development of renewable energy conversion and storage technologies, including fuel cells and metal-air batteries, where the cathodic oxygen reduction reaction (ORR) plays a pivotal role.[1,2] However, the poor kinetic characteristics of the available ORR materials has impeded any practical realization of the related applications on an industrial scale. Platinum group metal (PGM) catalysts have been used to address the difficulties associated with ORR operation, but the poor availability and high cost of PGMs make their widespread usage impractical.[3] Based on their low cost, high activities, and excellent stabilities, nitrogen-doped porous carbons incorporating transition metals (Fe, Cu, Co, and Ni) in different states are promising replacement materials for Pt-based ORR systems.[4–10] In these materials, the introduction of different metal-nitrogen ($M\text{-}N_x$) coordination sites is a critical factor in determining their overall efficiency, and also helps establish structure-activity relationships.[11–14] $M\text{-}N_x$ coordination sites can be conveniently introduced to the relevant materials by using appropriate coordination complexes such as porphyrins or phthalocyanines, which provide four nitrogen atoms in an $M\text{-}N_x$ coordination structure with a suitable geometry not only to bind transition metal cations but also to maintain a state of coordination unsaturation.[15,16] While $M\text{-}N_x$ porphyrins and phthalocyanines have been incorporated into different materials for the construction of various composite electrocatalysts,[17–22] there remain several disadvantages associated with this approach including their low affinity for the conductive scaffolds and their strong tendency to aggregate, both of which lead to poor charge and mass transfer rates, low mass efficiency, and low stability of the resulting materials. $M\text{-}N_x$-type molecules can also be incorporated as linkers or monomers in the construction of metal-organic framework (MOFs),[23,24] covalent organic polymers (COPs)[25–29] or covalent organic frameworks (COFs).[30,31] Porous porphyrin polymers

have also been studied for the construction of M-N_x systems[32–35] with the resulting nitrogen-doped carbon materials being porous and conductive promoting their usefulness in oxygen reduction reaction (ORR) applications. In addition, the use of N-doped graphene supports containing pyridinic N or graphitic N states can enhance the oxygen reduction reaction (ORR) performance of the relevant materials,[36,37] and the use of highly porous conducting carbon supports having numerous exposed active sites facilitates electrocatalytic reactions.

Other important potential components of oxygen reduction electrocatalysts are based on cobalt compounds whose electrochemical activities have been enhanced by preparing innovative architectures,[38–40] introduction of heteroatoms including boron,[41] nitrogen,[42,43] sulphur,[39,44–46] and/or oxygen,[47] or by the preparation of multimetallic systems.[45,48–51] The construction of single-atom catalysts (SACs) with multiple active sites also offers a promising strategy to improve ORR performance, while the use of multiple metal sites (including clusters or nanoparticles) anchored on N-doped carbon substrates allows optimized adsorption-desorption behavior during ORR due to synergistic effects between the metal sites and locally unsymmetrically distributed electron density.[49,52,53] Consequently, the copresence in the relevant materials of single metal atoms and nanoparticles holds significant potential for the optimization of ORR catalytic performance. However, an easily implementable approach to synthesize these materials based on combining single atom catalysts and metal nanoparticles on conducting N-doped graphene is lacking.

In this work, we have developed a simple synthesis protocol to prepare cobalt-based electrocatalysts based on an inexpensive porous porphyrin polymer precursor. Porous porphyrin polymer containing multiple transition metal binding sites is prepared in high yield using Friedel-Crafts cross-coupling polymerization of *meso*-tetraphenylporphyrin (TPP). Subsequently, cobalt cations are introduced by coordination in the porphyrin polymer. Controlled thermolysis of the resulting metallated porphyrin polymer results in materials

incorporating face-centered cubic (fcc) metallic cobalt nanoparticles (**Co-NP**) as well as cobalt single-atom catalysts (**Co-SA**) confined in porous N-doped graphitic carbon (**NPC**), which has been confirmed by using transmission electron microscopy (TEM), X-ray photoelectron spectroscopy (XPS), and other X-ray absorption techniques (XANES, EXAFS). Of the materials prepared, the **Co-NP**/**Co-SA**@**NPC** electrocatalyst exhibits remarkable oxygen reduction reaction (ORR) performance with an onset potential (E_{onset}) of 0.96 V vs RHE and a half-wave potential ($E_{1/2}$) of 0.865V vs RHE, surpassing the performances of control samples and the state-of-the-art reference material Pt/C (20 wt%). **Co-NP**/**Co-SA**@**NPC** catalyst also exhibits substantial methanol tolerance during operation, emphasizing its superiority over Pt/C, and has high durability making it an excellent candidate for implementation in the relevant applications.

Results and Discussion

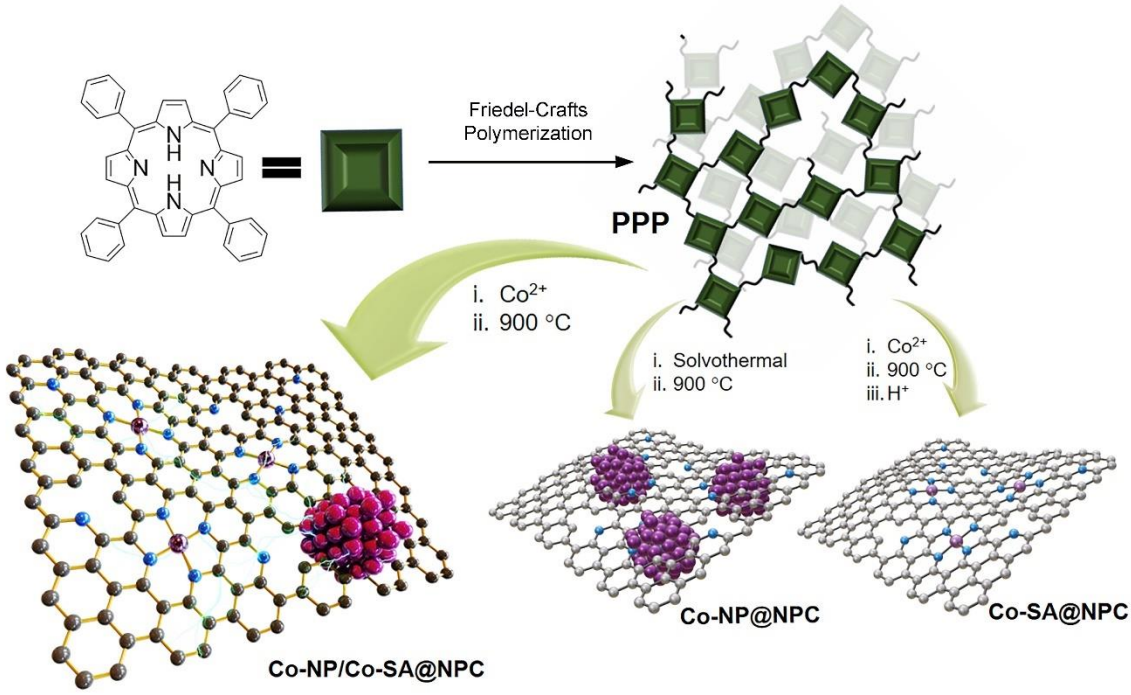

Fig. 1. Preparation of cobalt nanoparticle/cobalt single atom catalyst incorporated in nitrogen doped mulilayered graphitic carbon.

Porous porphyrin polymer (**PPP**) was prepared using *meso*-tetraphenylporphyrin (**TPP**) monomer by aryl-aryl Scholl coupling/solvent knitting Friedel-Crafts polymerization using aluminum chloride as Lewis acid catalyst in dichloromethane (See Fig. 1).[54] The reaction gives an insoluble brown powder as product, whose infrared spectrum (FT-IR; Fig. S1) contains broadened absorption bands signifying the polymeric structure of **PPP**. Cobalt cations were introduced to **PPP** by its reaction with $CoCl_2.6H_2O$ in refluxing DMF yielding **PPP-Co** confirmed by the appearance of the characteristic N-Co stretching vibration band at 1004 cm^{-1} in its FTIR spectrum.[55] **PPP-Co** was subjected to thermolysis under constant nitrogen gas flow at different temperatures in the range 500 – 1000 ºC. Cobalt nanoparticle (**Co-NP)**/cobalt single atom (**Co-SA**) catalytic sites deposited in nitrogen doped porous graphitic carbon (**NPC**) **Co-NP/Co-SA@NPC** materials were obtained upon thermolyzing **PPP-Co** at 1000 °C. Free base porphyrin polymer thermolyzed under the same conditions (**PPP-1000**), cobalt single-atom-

only **Co-SA@NPC** and cobalt nanoparticle-only **Co-NP@NPC** (prepared by solvothermal treatment) in nitrogen doped porous carbon were also prepared as control materials for comparative purposes.

Surface areas and porosities of the materials were measured using nitrogen adsorption/desorption isotherms. (Fig. S2a) The relatively large adsorption of nitrogen at 77 K at low relative pressure (P/P_0 0.01) for **PPP, PPP-Co** indicates that micropores contribute significantly to the total pore volume. Following thermolysis, there is a predictable decline in the surface area due to the partial collapse of the porous structure, although a substantial surface area is retained; **Co-NP/Co-SA@NPC** maintained 478 $m^2\ g^{-1}$ while **PPP-Co** maintained 970 $m^2\ g^{-1}$. Variation in surface area of **Co-NP/Co-SA@NPC** with increasing temperature corresponds approximately to the weight-loss according to thermogravimetry (Fig S2b) The excellent acid/base and thermal stability (more than 85% mass remains after pyrolysis) and retention of the porous structure can be attributed to the robust network aromatic polymer structure, which provides an additional advantage over, for instance, materials prepared by direct pyrolysis of the porphyrin monomer.[56] The large surface areas and tailored pore size distributions of the materials are favorable to promote electrochemical processes, in particular facilitating ion diffusion.

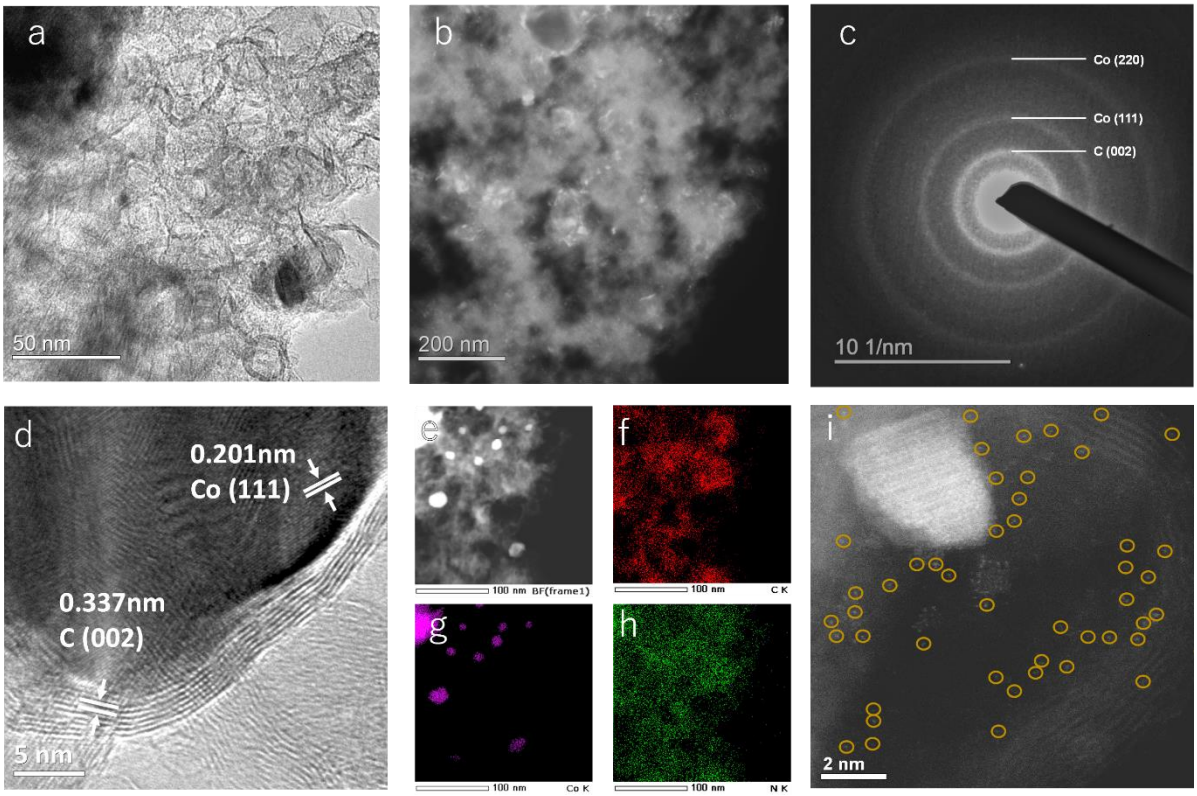

Fig. 2. Electron microscopy analyses of **Co-NP/Co-SA@NPC**. (a) Scanning transmission electron microscopy (STEM) image (bright field mode). (b) STEM image (dark field). (c) Selected area electron diffraction (SAED) pattern with indices. (d) High resolution TEM image with important lattice fringes indicated for C and Co. (e) STEM and (f-h) EDX elemental mapping of the area shown in (e). (i) Aberration-corrected high-angle annular dark-field scanning transmission electron microscopy (ac-HAADF-STEM) images of Co-NP/Co-SA@NPC. Sites of single Co atoms are marked with yellow circles.

Morphological analyses of the materials are shown in Fig. 2 and Fig. S3-S5 in the Supporting Information. Scanning electron microscopy (SEM; Fig. S3) reveals an irregular aggregated particle structure of the polymers, a morphology that hardly varies during metalation and thermolysis. Transmission electron microscopy (TEM) images (Fig. S4) of **PPP-Co** indicate that there are no cobalt nanoparticles present and selected area electron

diffraction (SAED) patterns contain no reflections because the polymers are amorphous with no long-range crystallographic order due to their irregular chemical structure.[26] Energy-dispersive X-ray spectroscopy (EDX; Fig. S6) confirms the presence of C, N, and Co distributed uniformly in **PPP-Co**. TEM imaging of **Co-NP/Co-SA@NPC** (Fig. 2a) reveals its nanometric porous morphology and the STEM image (Fig. 2b) contains bright spots due to the presence of cobalt nanoparticles (**Co-NP**) in the carbon matrix. The selected area electron diffraction (SAED) pattern (Fig. 2c) contains (111) and (220) planes assigned to *fcc* **Co-NP**s. EDX (Fig. 2d-g) of **Co-NP/Co-SA@NPC** establishes the presence of Co (apparently in nanoparticulate form) and a uniform distribution of N consistent with the proposed structure: **Co-NP** embedded in N-doped carbon. HR-TEM imaging (Fig. 2h) reveals that Co-NPs are coated with layers of graphitic carbon and the lattice fringes at 0.34 and 0.20 nm can be assigned to (002) interplane distances of graphitic carbon and the (111) plane of metallic Co, respectively, the latter which supports the formation of **Co-NP**. **Co-NP**s catalyze the conversion of amorphous carbon to graphitic carbon during the high temperature thermolysis process thus improving intercomponent electron transfer with graphitic carbon also acting as a protective barrier preventing aerial oxidation of metallic cobalt of **Co-NPs**.[57] Atom-level structural features of **Co-NP/Co-SA@NPC** were investigated using aberration-corrected high-angle annular dark-field scanning TEM (ac-HAADF-STEM). As shown in Fig. 2i, a moderate number of scattered bright dots (indicated by yellow circles, see also Fig. S5) are present corresponding to cobalt single atom (**Co-SA**) sites (identified as being CoN_4 species; vide infra) distributed throughout the carbon matrix. HR-TEM (Fig. S5a) of **Co-SA@NPC** shows graphitic nanorings about pores formed by acid etching of the cobalt nanoparticles. For comparison, see Fig. S5b where **Co-NP** immobilized between several layers of graphitic carbon can be observed for **Co-NP@NPC**. Lattice fringes consistent with the proposed structures were observed at 0.21 and 0.34 nm respectively corresponding to Co(111) and

graphitic C(002). **PPP-Co** exhibited no SAED or XRD peaks consistent with its essentially amorphous structure and lack of **Co-NP**.

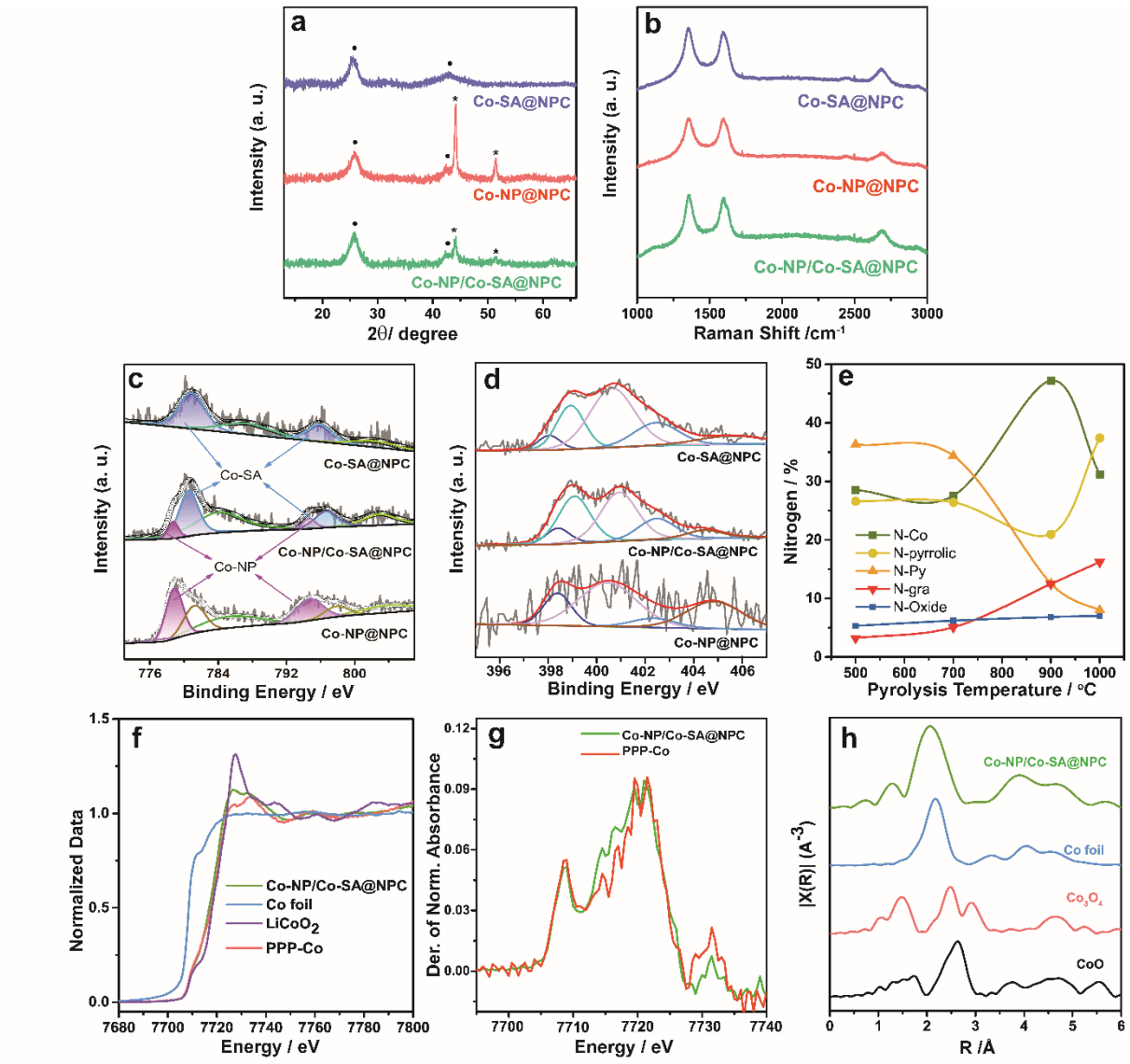

Fig. 3. Spectroscopic analyses of different **Co-NP/Co-SA@NPC** materials. (a) Powder X-ray diffraction (pXRD) patterns. (b) Raman spectra. (c,d) High resolution X-ray photoelectron spectroscopy (XPS) spectra of **Co-NP/Co-SA@NPC**, **Co-SA@NPC**, **Co–NPC**: (c) Co2p (d) N1s. (e) Temperature dependency of nitrogen content of **PPP-Co**. (f) Normalized K-edge XANES spectra, (g) first derivative XANES spectra. (h) FT-EXAFS spectra of **Co-NP/Co-SA@NPC** and standard samples.

Other salient analyses of the materials are shown in Fig. 3. The PXRD pattern of **Co-NP/Co-SA@NPC** (Fig. 3a) contains two broad peaks at 26° and 43° due to the (002) and (101)

lattice planes of graphitic carbon.[58] Peaks at 44.1° and 51.4° are respectively associated with the (111) and (200) planes of metallic *fcc* **Co-NP** (JCPDS No. 15-0806). Peaks due to **Co-NP** are absent in samples pyrolyzed below 1000 °C indicating that nanoparticle formation occurs only at or above this temperature. Graphitic carbon peaks are also absent in samples thermolyzed between 500-700 °C indicating the importance of higher temperature (900 °C and above) for graphitization (Fig. S6a) Additionally, absence of graphitic structures in **PPP-1000** suggests that cobalt promotes graphitization.(Fig. S7) The pXRD pattern of **Co-NP@NPC** is similar to that of **Co-NP/Co-SA@NPC** indicating the presence of graphitic carbon and **Co-NP**, and the pXRD pattern of **Co-SA@NPC** contains only broad peaks assignable to graphitic carbon confirming the absence of **Co-NP**. Thus, the form and composition of **Co-NP/Co-SA@NPC** is strongly affected both by the presence of cobalt and by the thermolysis temperature, which both promote graphitization.

Raman spectra of the materials (Fig. 3b) contain two intense peaks around 1350 and 1580 cm^{-1} assigned as D and G bands, respectively ('D' indicates disordered carbon, 'G' is due to in-plane vibrations of sp^2 graphitic carbon). An additional peak at 2750 cm^{-1} corresponds to the 2D band of multilayered graphitic structures.[59] Materials thermolyzed below 1000 °C or without Co contained very weak or no 2D peak confirming the necessity of the two conditions for the formation of the multilayered graphitic structure. Raman spectra of **Co-SA@NPC** and **Co-NP@NPC** similarly contain D, G and 2D bands. The relative intensity ratio of D and G (I_d/I_g) indicates the degree of disorder in the carbon structure with values of 1.02, 1.01 and 1.0 calculated for **Co-SA@NPC**, **Co-NP/Co-SA@NPC** and **Co-NP@NPC** respectively. The small increase in I_d/I_g is due to nanoparticle formation.[60,61]

To gain insight into the chemical composition and oxidation states of the materials' components, X-ray photoelectron spectroscopy XPS measurements were performed. Peaks due to carbon, nitrogen and cobalt are found in the XPS survey spectrum. Fig. S8a shows the XPS

survey spectrum of **PPP-Co** including Co $2p_{1/2}$ and Co $2p_{3/2}$ at 795.7 and 780.3 eV, respectively (Fig. S8b). The N1s spectrum (Fig. S8c) is dominated by a peak at 399.16 eV peak which corresponds to the nitrogen-cobalt coordinate bond.[58] Fig. 3c,d shows the high-resolution Co 2p and N 1s XPS spectra of **Co-NP/Co-SA@NPC** where peaks at 778.7 and 794.6 eV correspond to Co 2p3/2 and 2p1/2 of metallic cobalt Co^0. Peaks at 780.5 and 796.4 eV correspond to Co^{2+} at cobalt single atom sites (CoN_4) with those at 784.04 and 802.8 eV being shakeup satellite peaks. Samples thermolyzed at lower temperatures and **Co-SA@NPC** contained no XPS peaks due to metallic Co consistent with the absence of nanoparticles found by pXRD. (Fig. S7) XPS spectra of **Co-NP@NPC** contain peaks due to metallic cobalt (**Co-NP**) at 778.7 and 794.6eV for Co $2p_{3/2}$ and Co $2p_{1/2}$, respectively. The XPS spectrum of **Co-NP/Co-SA@NPC** was deconvoluted with five peaks (Fig. 3d) at 398.4, 399.1, 400.9, 402.5, 404.4 eV corresponding respectively to pyridinic N, N-Co, pyrrolic nitrogen, graphitic nitrogen, N oxide, confirming nitrogen coordination of cobalt at single atom sites. (Fig. S9) Variation in the nitrogen contents with increasing temperature (Fig. 3e) revealed a decrease in N-Co and an increase in pyrrolic nitrogen above 900 °C due to aggregation of cobalt as cobalt nanoparticles and the resulting decline in availability of **Co-SA** single atom sites. An increase in the graphitic nitrogen content is found as the temperature increases from 500-900 °C (Fig. S10a). Interestingly, in the case of **Co-NP@NPC**, nitrogen content was found to be significantly reduced. This is likely due to loss of nitrogen during thermolysis due to the absence of single atom sites where the nitrogen might be retained in **NPC**. Furthermore, the absence of an N-Co peak confirms the absence of single-atom catalysts in **Co-NP@NPC**. In contrast, deconvolution of the nitrogen peaks in **Co-SA@NPC** revealed a similar pattern to that of **Co-NP/Co-SA@NPC** due to the retention of nitrogen in the structure and cobalt single atoms after etching of cobalt nanoparticles.

To investigate the electronic structure and coordination environment of **Co-NP/Co-SA@NPC** at the atomic level, X-ray absorption near-edge structure (XANES) and extended X-ray absorption structure (EXAFS) experiments were conducted at the Co K-edge. Fig. 3f shows the XANES spectrum of **Co-NP/Co-SA@NPC** which has a characteristic Co K-edge absorption located between those of Co foil and $LiCoO_2$ indicating Co oxidation states ranging from Co^0 to Co^{2+}. Furthermore, the first derivative of the XANES pre-edge data (Fig. 3g) shows a distinctive peak in the energy range 7710 to 7715 eV, corresponding to the $1s \rightarrow 4p^z$ transition of in-plane Co^{II}-N_4 moieties.[62] The EXAFS spectrum (Fig. 3h) contains a characteristic peak due to Co^0-Co^0 bonds configured at 2.1 Å, which further confirms the presence of Co metallic nanoparticles. A characteristic Co-N peak was also observed at 1.37 Å. A slight shift in the Co^0-Co^0 peak (relative to Co foil) in EXAFS and a XANES peak 7727eV for **Co-NP/Co-SA@NPC** is probably due to the strong interaction between **Co-NP** and **Co-SA** sites. Overall, the physical and chemical analyses suggest a close integration of cobalt single atom species and metallic cobalt nanoparticle in **Co-NP/Co-SA@NPC** which is combined within a graphitic porous structure. These are key features of **Co-NP/Co-SA@NPC** to promote its catalytic activity for ORR with a strong likelihood for the occurrence of synergetic effects.[63,64]

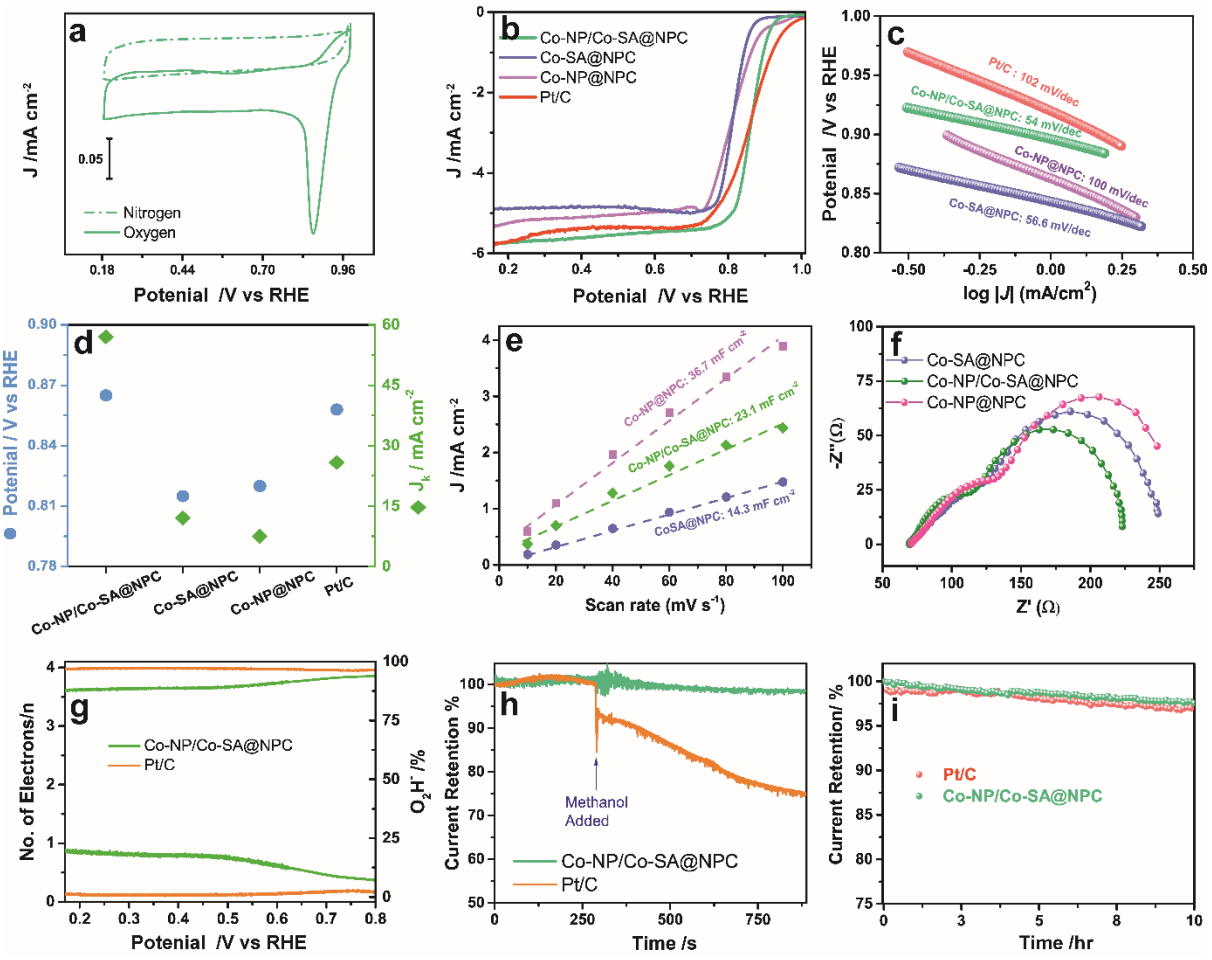

Fig. 4. Electrochemical characterization of **Co-NP/Co-SA@NPC**. (a) Cyclic voltammograms under N_2 (dashed line) and O_2 (solid line). (b) Linear sweep voltammetry (LSV) curves and (c) corresponding Tafel plots. (d) $E_{1/2}$ and J_k for the materials and Pt/C. (e) Electrical double layer capacitance, C_{dl} (f) Nyquist plot of the electrocatalysts at 1600 rpm in a 0.1 M KOH electrolyte. (g) $\%HO_2^-$and electron transfer number determined by RRDE at a scan rate of 10 mV s^{-1}. (h) Methanol crossover and (i) evaluation of durability based on the i–t chronoamperometric responses of **Co-NP/Co-SA@NPC** and **Pt/C**.

ORR catalytic activities of the **Co-NP/Co-SA@NPC** catalyst and other materials were evaluated by using electrochemical methods (Fig. 4) Cyclic voltammetry (CV) of **Co-NP/Co-SA@NPC** measurements at a scan rate of 25 mV s^{-1} in 0.1 M KOH solution (Fig. 4a) in nitrogen or oxygen saturated electrolyte using a three-electrode setup. For N_2 saturated electrolyte, no significant redox peaks were observed. However, for O_2 saturated electrolyte, a

strong cathodic response was observed demonstrating the excellent intrinsic catalytic activity of **Co-NP/Co-SA@NPC** catalyst for ORR. To further investigate, linear sweep voltammetry (LSV; Fig. 4b, Table S1) was conducted in an oxygen-saturated 0.1 M KOH solution using a rotating disk electrode (RDE) as the working electrode. Optimum thermolysis temperature for the materials was determined by comparing the ORR performance of electrocatalysts prepared at different temperatures. (Fig. S11, Table S2) Of the materials prepared, **Co-NP/Co-SA@NPC** prepared at 1000 °C, exhibits superior ORR catalytic performance with an onset potential (E_{onset}) of 0.96 V vs RHE (reversible hydrogen electrode) and a half-wave potential ($E_{1/2}$) of 0.865 V vs RHE, the latter value being similar to **Pt/C** (20 wt%). However, as observed from the polarization curve, the mixed (kinetic + diffusion) region potential window for **Co-NP/Co-SA@NPC** is narrower than that of **Pt/C**. Of the other materials tested, **PPP-Co** and **PPP-Co/500** exhibit low ORR activity due to ineffective development of the materials' structures especially a lack of graphitization. **PPP-1000** (Fig. S12) shows a 75 mV lower halfwave potential compared to **Co-NP/Co-SA@NPC** reflecting the importance of cobalt for efficient electrocatalysis by boosting ORR activity.

The effects of cobalt single atoms and nanoparticles were studied using the control electrocatalysts, **Co-SA@NPC** and **Co-NP@NPC**. Considering the LSV curves (Fig. 4b), it was found that **Co-NP/Co-SA@NPC** exhibits a 50 mV more positive half-wave potential than **Co-SA@NPC** (0.815 V vs RHE) indicating that cobalt nanoparticles enhance significantly the electrocatalytic activity. $E_{1/2}$ of nanoparticle only **Co-NP@NPC** is 45 mV lower than **Co-NP/Co-SA@NPC** emphasizing the importance also of the copresence of cobalt single atoms and cobalt nanoparticles including possible synergetic effects. The excellent ORR activity of **Co-NP/Co-SA@NPC** can be further confirmed by Tafel plots (Fig. 4c) and considering kinetic current density (J_k). As shown in Fig. 4d, **Co-NP/Co-SA@NPC** exhibits an excellent J_k value of 57 mA/cm^2 at 0.8 V, which is more than double that of **Pt/C**. Also, the Tafel slope of **Co-**

NP/Co-SA@NPC is 54.5 mV dec^{-1}, significantly lower than that of **Pt/C** (102 mV dec^{-1}), suggesting a significantly faster electron transfer rate for **Co-NP/Co-SA@NPC** (Fig. 4c) Interestingly, **Co-SA@NPC** has a Tafel slope (56.6 mV dec^{-1}) similar to **Co-NP/Co-SA@NPC**, while that of **Co-NP@NPC** (100 mV dec^{-1}) denotes comparatively slow electron transfer and is similar to Pt/C. This suggests that, while both **Co-SA** and **Co-NP** improve ORR efficiency, the role of **Co-SA** is to increase electron transfer rate.

Intrinsic electrocatalytic activity was investigated using impedance spectroscopy and electrochemical double layer capacitance (C_{dl}) based on the cyclic voltammetry (CV) curves at different scan rates. (Fig. S13) **Co-NP/Co-SA@NPC** exhibits a high C_{dl} value of 23 mF cm^{-2}, indicating a larger electrochemical surface area than for **Co-SA@NPC** (C_{dl} = 14.3 mF cm^{-2}), although it is lower than that of **Co-NP@NPC** (C_{dl} = 36.7 mF cm^{-2}).(Fig. 4e) This indicates a larger number of catalytically active sites for **Co-NP/Co-SA@NPC** over **Co-SA@NPC** due to the etching of cobalt nanoparticles. Nyquist plots of the materials (Fig. 4f) indicate that **Co-NP/Co-SA@NPC** has the lowest charge transfer resistance (58 Ω), compared to **Co-NP@NPC** (91.4Ω) and **Co-SA@NPC** (90.18Ω) suggesting faster charge transfer than occurs in the other materials under the same conditions.

Rotating ring disk electrode (RRDE) tests (Fig. 4g) show an electron transfer number for ORR by **Co-NP/Co-SA@NPC** at 3.8, indicating a nearly four-electron pathway for ORR. Notably, the peroxide yield calculated for **Co-NP/Co-SA@NPC** is 14.9 %, within the potential window 0.2 to 0.8 V. Compared to other cobalt electrocatalysts derived from porphyrins, [56,65,66] **Co-NP/Co-SA@NPC** exhibits a higher electron transfer number and lower peroxide yield, probably based on the presence of cobalt nanoparticles. As expected, **Co-SA@NPC** also shows a higher peroxide yield compared to **Co-NP/Co-SA@NPC** further confirming that cobalt single atom sites from the porphyrin moiety tends weakly to the two-electron pathway for ORR.

To elucidate the direct involvement of single atom active sites in promoting the ORR activity, a poisoning test was performed using NaCN which is known to block M–Nx centers.[67,68] As shown in Fig. S14, poisoning leads to a decrease in the halfwave potential and limiting current density for **Co-NP/Co-SA@NPC, Co-NP@NPC** and **Co-SA@NPC**. **Co-NP/Co-SA@NPC** undergoes an 86 mV drop in its halfwave potential; for **Co-SA@NPC**, a 69 mV reduction is observed. Also, it is interesting to note that the reduction in diffusion limited current is prominent for **Co-SA@NPC** (27% drop) and **Co-NP@NPC** (13.7%) compared to **Co-NP/Co-SA@NPC** (7.5% drop), suggesting excellent poisoning tolerance of the electrocatalyst. Poisoning tolerance might arise from a higher density of active sites, which can compensate for the losses caused by poisoning. Additionally, the graphitic carbon structure provides a physical barrier, preventing direct contact between the poisoning agent and the active sites. These results suggest that the high ORR activity of **Co-NP/Co-SA@NPC** can be attributed to a synergetic effect, due to the copresence of single atom centers and cobalt nanoparticles. Methanol tolerance and durability of the catalyst are also important aspects for practical implementation of the catalyst. Fig. 4h shows that **Co-NP/Co-SA@NPC** maintains a stable current density even after injection of 3 M methanol, whereas **Pt/C** exhibits a sharp decrease in current density due to methanol oxidation. Additionally, as shown in Fig. 4i, **Co-NP/Co-SA@NPC** retains a significant percentage of its initial current density after 10 h of continuous operation, indicating the excellent durability of the catalyst. High durability of the catalyst is attributed to its resistance to peroxide and effective protection especially of the Co-NP sites provided by the multilayered graphitic structure. The remarkable methanol tolerance and excellent durability of the **Co-NP/Co-SA@NPC** electrocatalyst along with superior performance compared to other cobalt based catalysts (Table S3) highlight its strong potential for practical applications.

Although **Co-NP/Co-SA@NPC** is a mixed component material having a broad range of environments for each of its active elements including wide-ranging separating distances of the active sites, we have assessed their relative contributions, especially **Co-NP** and **Co-SA**, using computational methods. In particular, synergies between active sites are not easy to detect even if experimental data indicates that such mechanisms are operating. For computational purposes, an N-doped graphene (**NPC**) structure containing the three most common nitrogen defects observed in graphene (pyrrolic, pyridinic and graphitic) was constructed (see Figure S15a). Cobalt single atom catalyst (**SA**) sites can be formed by incorporating a Co atom into a void provided by an N_4 defect (Figure S15b), which represents a remnant of the starting porphyrin materiaal. A thirteen Co atom icosahedral nanoparticle was also constructed using the Atomic Simulation Environment (ASE) toolkit and was incorporated on **NPC**. The formation energies of **NPC** and **Co-SA** on N-doped graphene (**Co-SA@NPC**) and **Co-NP** on **NPC** (**Co-NP@NPC**) were calculated using the following equations:

$$E_f\ (\mathbf{NPC}) = E_{total}\ (\mathbf{NPC}) - E(\text{graphene}) - 3.5 * E(N_2) \quad [1]$$

$$E_f\ (\mathbf{Co\text{-}SA@NPC}) = E_{total}\ (\mathbf{Co\text{-}SA@NPC}) - E_{total}(\mathbf{NPC}) - E(\mathbf{Co}) \quad [2]$$

$$E_f(\mathbf{Co\text{-}NP@NPC}) = E_{total}(\mathbf{Co\text{-}NP@NPC}) - E_{total}\ (\mathbf{NPC}) - E_{icosahedron}(\text{Co}) \quad [3]$$

where, E_{total} (**NPC**), E_{total} (**Co-SA@NPC**) and E_f (**Co-NP@NPC**) are the total energies obtained during relaxation of **NPC**, **Co-SA@NPC** and **Co-NP@NPC** structures, respectively. $E(N_2)$, E(Co) and $E_{icosahedron}$(Co) are the energies of nitrogen molecules, Co atom in the nanoparticle structure and one unit of Co_{13} icosahedron, respectively. E_f (**NPC**), E_f (**Co-SA@NPC**) and E_f(**Co-NP@NPC**) are the formation energies of **NPC**, **Co-SA@NPC** and **Co-NP@NPC**, respectively.

To study the oxygen reduction reaction (ORR) activity on the resulting systems, an associative mechanism involving a $4e^-$ transfer process in alkaline medium was explored[69]:

$O_2(g) + * \rightarrow O_2*$ [4]

$O_2* + H_2O\ (l) + e^- \rightarrow HOO* + OH^-$ [5]

$HOO* + e^- \rightarrow O* + OH^-$ [6]

$O* + H_2O\ (l) + e^- \rightarrow HO* + OH^-$ [7]

$HO* + e^- \rightarrow OH^- + *$ [8]

Initially, the key intermediates for ORR reaction O*, OH* and OOH* are adsorbed on **Co-SA@NPC** at five distinct sites, namely C1, C2, C3, C4 and C5 (Figure 15b). The adsorption energies for all five sites were calculated using the following equations:

$$\Delta E_{ads}(HOO*) = E_{total}(HOO*) - [E* + 2E(H_2O) - 1.5E(H_2)] \quad [9]$$

$$\Delta E_{ads}(O*) = E_{total}(O*) - [E* + E(H_2O) - E(H_2)] \quad [10]$$

$$\Delta E_{ads}(HO*) = E_{total}(HO*) - [E* + E(H_2O) - 0.5E(H_2)] \quad [11]$$

where $\Delta E_{ads}(HO*)$, $\Delta E_{ads}(O*)$ and $\Delta E_{ads}(HOO*)$ are the adsorption energies of HO*, O* and HOO* intermediates, respectively. $E_{total}(HO*)$, $E_{total}(O*)$ and $E_{total}(HOO*)$ are the total energies of the system, E* is the energy of the system without intermediate, $E(H_2O)$ and $E(H_2)$ are the energy of the reference molecules.

Figure S16 shows adsorption energy profile of ORR intermediates adsorbed over five distinct sites. However, the adsorption energy is quite high for all the cases. This is expected because of the electronegative nature of nitrogen which inhibits adsorption on carbon as well as at Co. In view of these matters, new structures to study reactions on **Co–SA@NPC** and **Co-NP@NPC** were prepared (Figure S17) involving binding of **Co-SA** at a single pyridinic-N defect site. Intermediates species *OH, *O and *OOH were adsorbed over Co site in reconstructed **Co-SA@NPC** (Figure S17a) and reconstructed **Co-NP@NPC** (Figure S17b). The free energy profile is shown in Figure 5. Free energy of the O* intermediate over Co in **Co-NP@NPC** is lower than that in **Co-SA@NPC** (Figure 5) with Bader charges of –0.79 and –0.58, respectively (Table S3). Oxygen intermediate is strongly bound at the hollow site

formed by three cobalt atoms of **Co-NP** (Figure S18). Hence, it experiences greater charge accumulation than its **Co-SA** counterpart. Similarly, O atoms in HO* and HOO* intermediates are saturated with three Co atoms (Figure S18). This saturation leads to stronger interaction of these intermediates with **Co-NP** making desorption difficult. This is reflected in the free energy plots where overpotential for **Co-NP@NPC** is greater than for **Co-SA@NPC**. However, both systems show negative free energy at U = 1.23 V. Hence, structures comprising **Co-SA** and **Co-NP** can accelerate the ORR process more effectively than the individual systems.

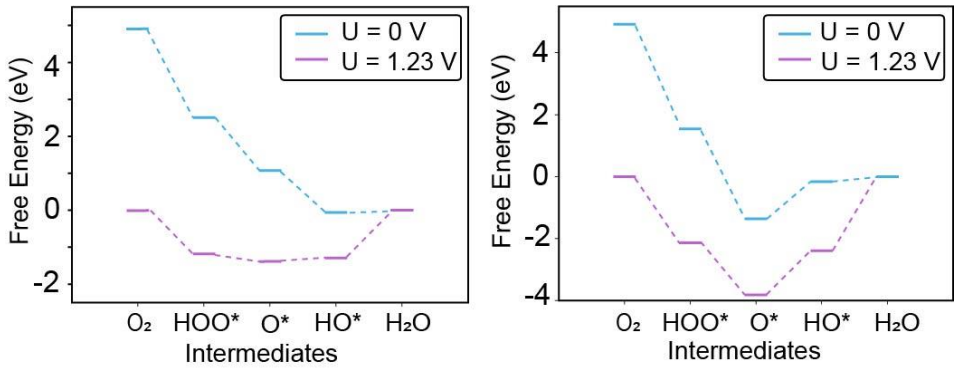

Figure 5. Gibbs free energy plots for oxygen reduction reaction for **Co-SAC@NPC** (left) and **Co-NP@NPC** (right).

Conclusion

In summary, we have developed a facile, low-cost synthesis of ORR-active electrocatalyst, which is not only highly scalable based on its ease of operation, but also produces poisoning-resistant materials with ORR performance ostensibly superior to Pt/C. The synthesis protocol involves Friedel-Crafts polymerization/metalation/thermolysis and leads to the electrocatalyst **Co-NP/Co-SA@NPC** consisting of N-doped graphene embedded with single cobalt atoms in the copresence of cobalt nanoparticles and with an ultralow loading of Co (0.3 at%). The composition of the material has been investigated in-depth allowing a deeper understanding of its electrochemical properties and usefulness as an electrocatalyst.

Remarkably, **Co-NP/Co-SA@NPC** catalyst exhibits an ORR half-wave potential of 0.865 V vs RHE, surpassing the performance of commercial 20 wt% Pt/C catalyst and competitive with other reported ORR catalysts (see Table S4). Furthermore, the **Co-NP/Co-SA@NPC** electrocatalyst exhibits superior durability and methanol tolerance compared to Pt/C. Computational analysis supports possible synergetic effects in **Co-NP/Co-SA@NPC** where copresence of **Co-NP/Co-SA** can accelerate ORR processes. Overall, the scalable synthesis method and excellent properties of this catalyst paves the way for the future development of high-performance cobalt-based electrocatalysts for ORR in industrial applications, especially alkaline fuel cell devices.

Declaration of Competing Interests

The authors declare that there are no competing financial interests.

Acknowledgements

The authors are grateful to JST-ERATO Yamauchi Materials Space-Tectonics Project (JPMJER2003) and the Queensland Node of the Australian National Fabrication Facility (ANFF-Q). J.X. is grateful to the National Institute for Materials Science, International Center for Young Scientists, Japan (ICYS, NIMS) for an ICYS fellowship and research funds). This research was also partly supported by World Premier International Research Center Initiative (WPI Initiative), MEXT, Japan. N.V. is grateful for financial support from the Japan Society for the Promotion of Science (JSPS) for a JSPS postdoctoral fellowship (P21764) supported by JSPS KAKENHI Grant Number JP22KF0385.

References

1. Zhang, J.; Xia, Z.; Dai, L. Carbon-Based Electrocatalysts for Advanced Energy Conversion and Storage. *Sci. Adv.* **2023**, *1*, e1500564. DOI:10.1126/sciadv.1500564.

2. Seh, Z. W.; Kibsgaard, J.; Dickens, C. F.; Chorkendorff, I.; Nørskov, J. K.; Jaramillo, T. F. Combining Theory and Experiment in Electrocatalysis: Insights into Materials Design. *Science* **2017**, *355*, eaad4998. DOI:10.1126/science.aad4998.

3. Tian, X.; Zhao, X.; Su, Y.-Q.; Wang, L.; Wang, H.; Dang, D.; Chi, B.; Liu, H.; Hensen, E. J. M.; Lou, X. W.; Xia, B. Y. Engineering Bunched Pt-Ni Alloy Nanocages for Efficient Oxygen Reduction in Practical Fuel Cells. *Science* **2019**, *366*, 850–856. DOI:10.1126/science.aaw7493.

4. Zeng, R.; Yang, Y.; Feng, X.; Li, H.; Gibbs, L. M.; DiSalvo, F. J.; Abruña, H. D. Nonprecious Transition Metal Nitrides as Efficient Oxygen Reduction Electrocatalysts for Alkaline Fuel Cells. *Sci. Adv.* **2023**, *8*, eabj1584. DOI:10.1126/sciadv.abj1584.

5. Zhou, Y.; Chen, G.; Wang, Q.; Wang, D.; Tao, X.; Zhang, T.; Feng, X.; Müllen, K. Fe-N-C Electrocatalysts with Densely Accessible Fe-N4 Sites for Efficient Oxygen Reduction Reaction. *Adv. Funct. Mater.* **2021**, *31*, 2102420. DOI:10.1002/adfm.202102420.

6. Jung, E.; Shin, H.; Lee, B.-H.; Efremov, V.; Lee, S.; Lee, H. S.; Kim, J.; Hooch Antink, W.; Park, S.; Lee, K.-S.; Cho, S.-P.; Yoo, J. S.; Sung, Y.-E.; Hyeon, T. Atomic-Level Tuning of Co–N–C Catalyst for High-Performance Electrochemical H2O2 Production. *Nat. Mater.* **2020**, *19*, 436–442. DOI:10.1038/s41563-019-0571-5.

7. Li, J.; Chen, M.; Cullen, D. A.; Hwang, S.; Wang, M.; Li, B.; Liu, K.; Karakalos, S.; Lucero, M.; Zhang, H.; Lei, C.; Xu, H.; Sterbinsky, G. E.; Feng, Z.; Su, D.; More, K. L.; Wang, G.; Wang, Z.; Wu, G. Atomically Dispersed Manganese Catalysts for Oxygen Reduction in

Proton-Exchange Membrane Fuel Cells. *Nat. Catal.* **2018**, *1*, 935–945. DOI:10.1038/s41929-018-0164-8.

8. Kong, Z.; Liu, T.; Hou, K.; Guan, L. Atomically Dispersed Mn–N4 Electrocatalyst with High Oxygen Reduction Reaction Catalytic Activity from Metal–Organic Framework ZIF-8 by Minimal-Water-Assisted Mechanochemical Synthesis. *J. Mater. Chem. A.* **2022**, *10*, 2826–2834. DOI:10.1039/D1TA09183B.

9. Li, J.; Xia, W.; Tang, J.; Gao, Y.; Jiang, C.; Jia, Y.; Chen, T.; Hou, Z.; Qi, R.; Jiang, D.; Asahi, T.; Xu, X.; Wang, T.; He, J.; Yamauchi, Y. Metal–Organic Framework-Derived Graphene Mesh: A Robust Scaffold for Highly Exposed Fe–N4 Active Sites toward an Excellent Oxygen Reduction Catalyst in Acid Media. *J. Am. Chem. Soc.* **2022**, *144*, 9280–9291. DOI:10.1021/jacs.2c00719.

10. Tan, H.; Tang, J.; Kim, J.; Kaneti, Y. V.; Kang, Y.-M.; Sugahara, Y.; Yamauchi, Y. Rational Design and Construction of Nanoporous Iron- and Nitrogen-Doped Carbon Electrocatalysts for Oxygen Reduction Reaction. *J. Mater. Chem. A* **2019**, *7*, 1380–1393. DOI:10.1039/C8TA08870E.

11. Yasuda, S.; Furuya, A.; Uchibori, Y.; Kim, J.; Murakoshi, K. Iron–Nitrogen-Doped Vertically Aligned Carbon Nanotube Electrocatalyst for the Oxygen Reduction Reaction. *Adv. Funct. Mater.* **2016**, *26*, 738–744. DOI:10.1002/adfm.201503613.

12. Usov, P. M.; Huffman, B.; Epley, C. C.; Kessinger, M. C.; Zhu, J.; Maza, W. A.; Morris, A. J. Study of Electrocatalytic Properties of Metal–Organic Framework PCN-223 for the Oxygen Reduction Reaction. *ACS Appl. Mater. Interfaces* **2017**, *9*, 33539–33543. DOI:10.1021/acsami.7b01547.

13. Jiang, R.; Li, L.; Sheng, T.; Hu, G.; Chen, Y.; Wang, L. Edge-Site Engineering of Atomically Dispersed Fe–N4 by Selective C–N Bond Cleavage for Enhanced Oxygen

Reduction Reaction Activities. *J. Am. Chem. Soc.* **2018**, *140*, 11594–11598. DOI:10.1021/jacs.8b07294.

14. Kim, M.; Firestein, K. L.; Fernando, J. F. S.; Xu, X.; Lim, H.; Golberg, D. V; Na, J.; Kim, J.; Nara, H.; Tang, J.; Yamauchi, Y. Strategic Design of Fe and N Co-Doped Hierarchically Porous Carbon as Superior ORR Catalyst: From the Perspective of Nanoarchitectonics. *Chem. Sci.* **2022**, *13*, 10836–10845. DOI:10.1039/D2SC02726G.

15. Bisen, O. Y.; Nandan, R.; Raj, G.; Yadav, A. K.; Nanda, K. K. Rational Designing of Co–N–C Electrocatalysts for Comprehensive Elucidation of Intrinsic and Extrinsic Activities in the Oxygen Reduction Reaction. *ACS Appl. Energy Mater.* **2022**, *5*, 14019 − 14034. DOI:10.1021/acsaem.2c02606.

16. Yabu, H.; Nakamura, K.; Matsuo, Y.; Umejima, Y.; Matsuyama, H.; Nakamura, J.; Ito, K. Pyrolysis-Free Oxygen Reduction Reaction (ORR) Electrocatalysts Composed of Unimolecular Layer Metal Azaphthalocyanines Adsorbed onto Carbon Materials. *ACS Appl. Energy Mater.* **2021**, *4*, 14380–14389. DOI:10.1021/acsaem.1c03054.

17. Wu, Y.; Jiang, Z.; Lu, X.; Liang, Y.; Wang, H. Domino Electroreduction of CO2 to Methanol on a Molecular Catalyst. *Nature* **2019**, *575*, 639–642. DOI:10.1038/s41586-019-1760-8.

18. Li, X.; Lei, H.; Liu, J.; Zhao, X.; Ding, S.; Zhang, Z.; Tao, X.; Zhang, W.; Wang, W.; Zheng, X.; Cao, R. Carbon Nanotubes with Cobalt Corroles for Hydrogen and Oxygen Evolution in PH 0–14 Solutions. *Angew. Chem. Int. Ed.* **2018**, *57*, 15070–15075. DOI:10.1002/anie.201807996.

19. Liberman, I.; Shimoni, R.; Ifraemov, R.; Rozenberg, I.; Singh, C.; Hod, I. Active-Site Modulation in an Fe-Porphyrin-Based Metal–Organic Framework through Ligand Axial

Coordination: Accelerating Electrocatalysis and Charge-Transport Kinetics. *J. Am. Chem. Soc.* **2020**, *142*, 1933–1940. DOI:10.1021/jacs.9b11355.

20. Fan, W.; Duan, Z.; Liu, W.; Mehmood, R.; Qu, J.; Cao, Y.; Guo, X.; Zhong, J.; Zhang, F. Rational Design of Heterogenized Molecular Phthalocyanine Hybrid Single-Atom Electrocatalyst towards Two-Electron Oxygen Reduction. *Nat. Commun.* **2023**, *14*, 1426. DOI:10.1038/s41467-023-37066-y.

21. Lei, H.; Liu, C.; Wang, Z.; Zhang, Z.; Zhang, M.; Chang, X.; Zhang, W.; Cao, R. Noncovalent Immobilization of a Pyrene-Modified Cobalt Corrole on Carbon Supports for Enhanced Electrocatalytic Oxygen Reduction and Oxygen Evolution in Aqueous Solutions. *ACS Catal.* **2016**, *6*, 6429–6437. DOI:10.1021/acscatal.6b01579.

22. Xia, W.; Hou, Z.; Tang, J.; Li, J.; Chaikittisilp, W.; Kim, Y.; Muraoka, K.; Zhang, H.; He, J.; Han, B.; Yamauchi, Y. Materials Informatics-Guided Superior Electrocatalyst: A Case of Pyrolysis-Free Single-Atom Coordinated with N-Graphene Nanomesh. *Nano Energy* **2022**, *94*, 106868. DOI:10.1016/j.nanoen.2021.106868.

23. Zhao, M.; Wang, Y.; Ma, Q.; Huang, Y.; Zhang, X.; Ping, J.; Zhang, Z.; Lu, Q.; Yu, Y.; Xu, H.; Zhao, Y.; Zhang, H. Ultrathin 2D Metal–Organic Framework Nanosheets. Adv. Mater. **2015**, *27*, 7372–7378. DOI:10.1002/adma.201503648.

24. Feng, D.; Gu, Z.-Y.; Li, J.-R.; Jiang, H.-L.; Wei, Z.; Zhou, H.-C. Zirconium-Metalloporphyrin PCN-222: Mesoporous Metal–Organic Frameworks with Ultrahigh Stability as Biomimetic Catalysts. *Angew. Chem. Int. Ed.* **2012**, *51*, 10307–10310. DOI:10.1002/anie.201204475.

25. Wang, R.; Wang, X.; Weng, W.; Yao, Y.; Kidkhunthod, P.; Wang, C.; Hou, Y.; Guo, J. Proton/Electron Donors Enhancing Electrocatalytic Activity of Supported Conjugated

Microporous Polymers for CO_2 Reduction. *Angew. Chem. Int. Ed.* **2022**, *61*, e202115503. DOI:10.1002/anie.202115503.

26. Xiang, Z.; Xue, Y.; Cao, D.; Huang, L.; Chen, J.-F.; Dai, L. Highly Efficient Electrocatalysts for Oxygen Reduction Based on 2D Covalent Organic Polymers Complexed with Non-Precious Metals. *Angew. Chem. Int. Ed.* **2014**, *53*, 2433–2437. DOI:10.1002/anie.201308896.

27. Chen, J.; Wu, D.; Zhou, Z.; Huang, Y. Improved Uniformity of Fe3O4 Nanoparticles on Fe–N–C Nanosheets Derived from a 2D Covalent Organic Polymer for Oxygen Reduction. *Int. J. Hydrogen Energy* **2021**, *46*, 27576–27584. DOI:10.1016/j.ijhydene.2021.05.202.

28. Li, X.; Xiang, Z. Identifying the Impact of the Covalent-Bonded Carbon Matrix to FeN4 Sites for Acidic Oxygen Reduction. *Nat. Commun.* **2022**, *13*, 57. DOI:10.1038/s41467-021-27735-1.

29. Liao, Z.; Wang, Y.; Wang, Q.; Cheng, Y.; Xiang, Z. Bimetal-Phthalocyanine Based Covalent Organic Polymers for Highly Efficient Oxygen Electrode. *Appl. Catal. B* **2019**, *243*, 204–211. DOI:10.1016/j.apcatb.2018.10.038.

30. Yuan, J.; Chen, S.; Zhang, Y.; Li, R.; Zhang, J.; Peng, T. Structural Regulation of Coupled Phthalocyanine–Porphyrin Covalent Organic Frameworks to Highly Active and Selective Electrocatalytic CO_2 Reduction. *Adv. Mater.* **2022**, *34*, 2203139. DOI:10.1002/adma.202203139.

31. Lin, S.; Diercks, C. S.; Zhang, Y.-B.; Kornienko, N.; Nichols, E. M.; Zhao, Y.; Paris, A. R.; Kim, D.; Yang, P.; Yaghi, O. M.; Chang, C. J. Covalent Organic Frameworks Comprising Cobalt Porphyrins for Catalytic CO_2 Reduction in Water. *Science* **2015**, *349*, 1208–1213. DOI:10.1126/science.aac8343.

32. Lei, H.; Zhang, Q.; Liang, Z.; Guo, H.; Wang, Y.; Lv, H.; Li, X.; Zhang, W.; Apfel, U.-P.; Cao, R. Metal-Corrole-Based Porous Organic Polymers for Electrocatalytic Oxygen Reduction and Evolution Reactions. *Angew. Chem. Int. Ed.* **2022**, *61*, e202201104. DOI:10.1002/anie.202201104.

33. Hijazi, I.; Bourgeteau, T.; Cornut, R.; Morozan, A.; Filoramo, A.; Leroy, J.; Derycke, V.; Jousselme, B.; Campidelli, S. Carbon Nanotube-Templated Synthesis of Covalent Porphyrin Network for Oxygen Reduction Reaction. *J. Am. Chem. Soc.* **2014**, *136*, 6348–6354. DOI:10.1021/ja500984k.

34. Li, B.-Q.; Zhang, S.-Y.; Wang, B.; Xia, Z.-J.; Tang, C.; Zhang, Q. A Porphyrin Covalent Organic Framework Cathode for Flexible Zn–Air Batteries. *Energy Environ. Sci.* **2018**, *11*, 1723–1729. DOI:10.1039/C8EE00977E.

35. Li, B.-Q.; Zhang, S.-Y.; Chen, X.; Chen, C.-Y.; Xia, Z.-J.; Zhang, Q. One-Pot Synthesis of Framework Porphyrin Materials and Their Applications in Bifunctional Oxygen Electrocatalysis. *Adv. Funct. Mater.* **2019**, *29*, 1901301. DOI:10.1002/adfm.201901301.

36. Zhu, J.; Zhou, H.; Zhang, C.; Zhang, J.; Mu, S. Dual Active Nitrogen Doped Hierarchical Porous Hollow Carbon Nanospheres as an Oxygen Reduction Electrocatalyst for Zinc–Air Batteries. *Nanoscale* **2017**, *9*, 13257–13263. DOI:10.1039/C7NR04349J.

37. Jia, Y.; Zhang, L.; Zhuang, L.; Liu, H.; Yan, X.; Wang, X.; Liu, J.; Wang, J.; Zheng, Y.; Xiao, Z.; Taran, E.; Chen, J.; Yang, D.; Zhu, Z.; Wang, S.; Dai, L.; Yao, X. Identification of Active Sites for Acidic Oxygen Reduction on Carbon Catalysts with and without Nitrogen Doping. *Nat. Catal.* **2019**, *2*, 688–695. DOI:10.1038/s41929-019-0297-4.

38. Liu, R.; von Malotki, C.; Arnold, L.; Koshino, N.; Higashimura, H.; Baumgarten, M.; Müllen, K. Triangular Trinuclear Metal-N4 Complexes with High Electrocatalytic Activity for Oxygen Reduction. *J. Am. Chem. Soc.* **2011**, *133*, 10372–10375. DOI:10.1021/ja203776f.

39. Han, C.; Li, Q.; Wang, D.; Lu, Q.; Xing, Z.; Yang, X. Cobalt Sulfide Nanowires Core Encapsulated by a N, S Codoped Graphitic Carbon Shell for Efficient Oxygen Reduction Reaction. *Small* **2018**, *14*, 1703642. DOI:10.1002/smll.201703642.

40. Yin, Y.; Wang, J.; Li, T.; Hill, J. P.; Rowan, A.; Sugahara, Y.; Yamauchi, Y. Nanoarchitecturing Carbon Nanodot Arrays on Zeolitic Imidazolate Framework-Derived Cobalt–Nitrogen-Doped Carbon Nanoflakes toward Oxygen Reduction Electrocatalysts. *ACS Nano* **2021**, *15*, 13240–13248. DOI:10.1021/acsnano.1c02950.

41. Yang, Z.; Yang, J.; Niu, H.; Hui, J.; Chen, H.; Xiang, M. Cobalt on Boron-Doped Carbon Nitride for a Novel Bifunctional Electrocatalyst in Zinc-Air Batteries. *Energy Storage* **2022**, *4*, e313. DOI:10.1002/est2.313.

42. Peng, L.; Sun, Y.; Guo, S.; Li, C. Correction: Highly Efficient Construction of Hollow Co–Nx Nanocube Cage Dispersion Implanted with Porous Carbonized Nanofibers for Li–O2 Batteries. *J. Mater. Chem. A* **2022**, *10*, 3820–3821. DOI:10.1039/D2TA90021A.

43. Xu, H.; Jia, H.; Li, H.; Liu, J.; Gao, X.; Zhang, J.; Liu, M.; Sun, D.; Chou, S.; Fang, F.; Wu, R. Dual Carbon-Hosted Co-N3 Enabling Unusual Reaction Pathway for Efficient Oxygen Reduction Reaction. *Appl. Catal. B* **2021**, *297*, 120390. DOI:10.1016/j.apcatb.2021.120390.

44. Lian, Y.; Shi, K.; Yang, H.; Sun, H.; Qi, P.; Ye, J.; Wu, W.; Deng, Z.; Peng, Y. Elucidation of Active Sites on S, N Codoped Carbon Cubes Embedding Co–Fe Carbides toward Reversible Oxygen Conversion in High-Performance Zinc–Air Batteries. *Small* **2020**, *16*, 1907368. DOI:10.1002/smll.201907368.

45. Li, W.; Wu, L.; Wu, X.; Shi, C.; Li, Y.; Zhang, L.; Mi, H.; Zhang, Q.; He, C.; Ren, X. Regulation and Mechanism Study of the CoS2/Cu2S-NF Heterojunction as Highly-Efficient Bifunctional Electrocatalyst for Oxygen Reactions. *Appl. Catal. B* **2022**, *303*, 120849. DOI:10.1016/j.apcatb.2021.120849.

46. Zhao, W.-W.; Bothra, P.; Lu, Z.; Li, Y.; Mei, L.-P.; Liu, K.; Zhao, Z.; Chen, G.; Back, S.; Siahrostami, S.; Kulkarni, A.; Nørskov, J. K.; Bajdich, M.; Cui, Y. Improved Oxygen Reduction Reaction Activity of Nanostructured CoS_2 through Electrochemical Tuning. *ACS Appl. Energy Mater.* **2019**, *2*, 8605–8614. DOI:10.1021/acsaem.9b01527.

47. Chaikittisilp, W.; Torad, N. L.; Li, C.; Imura, M.; Suzuki, N.; Ishihara, S.; Ariga, K.; Yamauchi, Y. Synthesis of Nanoporous Carbon–Cobalt-Oxide Hybrid Electrocatalysts by Thermal Conversion of Metal–Organic Frameworks. *Chem. Eur. J.* **2014**, *20*, 4217–4221. DOI:10.1002/chem.201304404.

48. Nandan, R.; Pandey, P.; Gautam, A.; Bisen, O. Y.; Chattopadhyay, K.; Titirici, M.-M.; Nanda, K. K. Atomic Arrangement Modulation in CoFe Nanoparticles Encapsulated in N-Doped Carbon Nanostructures for Efficient Oxygen Reduction Reaction. *ACS Appl. Mater. Interfaces* **2021**, *13*, 3771–3781. DOI:10.1021/acsami.0c16937.

49. Han, X.; Ling, X.; Yu, D.; Xie, D.; Li, L.; Peng, S.; Zhong, C.; Zhao, N.; Deng, Y.; Hu, W. Atomically Dispersed Binary Co-Ni Sites in Nitrogen-Doped Hollow Carbon Nanocubes for Reversible Oxygen Reduction and Evolution. *Adv. Mater.* **2019**, *31*, 1905622. DOI:10.1002/adma.201905622.

50. Sanad, M. F.; Puente Santiago, A. R.; Tolba, S. A.; Ahsan, M. A.; Fernandez-Delgado, O.; Shawky Adly, M.; Hashem, E. M.; Mahrous Abodouh, M.; El-Shall, M. S.; Sreenivasan, S. T.; Allam, N. K.; Echegoyen, L. Co–Cu Bimetallic Metal Organic Framework Catalyst Outperforms the Pt/C Benchmark for Oxygen Reduction. *J. Am. Chem. Soc.* **2021**, *143*, 4064–4073. DOI:10.1021/jacs.1c01096.

51. Bai, L.; Hsu, C.-S.; Alexander, D. T. L.; Chen, H. M.; Hu, X. A Cobalt–Iron Double-Atom Catalyst for the Oxygen Evolution Reaction. *J. Am. Chem. Soc.* **2019**, *141*, 14190–14199. DOI:10.1021/jacs.9b05268.

52. Huang, H.; Yu, D.; Hu, F.; Huang, S.-C.; Song, J.; Chen, H.-Y.; Li, L. L.; Peng, S. Clusters Induced Electron Redistribution to Tune Oxygen Reduction Activity of Transition Metal Single-Atom for Metal–Air Batteries. *Angew. Chem. Int. Ed.* **2022**, *61*, e202116068. DOI:10.1002/anie.202116068.

53. Yu, D.; Ma, Y.; Hu, F.; Lin, C.-C.; Li, L.; Chen, H.-Y.; Han, X.; Peng, S. Dual-Sites Coordination Engineering of Single Atom Catalysts for Flexible Metal–Air Batteries. *Adv. Energy Mater.* **2021**, *11*, 2101242. DOI:10.1002/aenm.202101242.

54. Msayib, K. J.; McKeown, N. B. Inexpensive Polyphenylene Network Polymers with Enhanced Microporosity. *J. Mater. Chem. A* **2016**, *4*, 10110–10113. DOI:10.1039/C6TA03257E.

55. Wu, Z.-S.; Chen, L.; Liu, J.; Parvez, K.; Liang, H.; Shu, J.; Sachdev, H.; Graf, R.; Feng, X.; Müllen, K. High-Performance Electrocatalysts for Oxygen Reduction Derived from Cobalt Porphyrin-Based Conjugated Mesoporous Polymers. *Adv. Mater.* **2014**, *26*, 1450–1455. DOI:10.1002/adma.201304147.

56. Orellana, W.; Loyola, C. Z.; Marco, J. F.; Tasca, F. Evidence of Carbon-Supported Porphyrins Pyrolyzed for the Oxygen Reduction Reaction Keeping Integrity. *Sci. Rep.* **2022**, 12 (1), 8072. DOI:10.1038/s41598-022-11820-6.

57. Zhang, M.; Wang, C.; Luo, R.; Zhang, W.; Chen, S.; Yan, X.; Qi, J.; Sun, X.; Wang, L.; Li, J. A Phenolic Resin-Assisted Strategy for MOF-Derived Hierarchical Co/N-Doped Carbon Rhombic Dodecahedra for Electrocatalysis. *J. Mater. Chem. A* **2019**, *7*, 5173–5178. DOI:10.1039/C8TA10918D.

58. Xiang, Z.; Xue, Y.; Cao, D.; Huang, L.; Chen, J.-F.; Dai, L. Highly Efficient Electrocatalysts for Oxygen Reduction Based on 2D Covalent Organic Polymers Complexed

with Non-Precious Metals. *Angew. Chem. Int. Ed.* **2014**, *53*, 2433–2437. DOI:10.1002/anie.201308896.

59. Kumar, P.; Kannimuthu, K.; Zeraati, A. S.; Roy, S.; Wang, X.; Wang, X.; Samanta, S.; Miller, K. A.; Molina, M.; Trivedi, D.; Abed, J.; Campos Mata, M. A.; Al-Mahayni, H.; Baltrusaitis, J.; Shimizu, G.; Wu, Y. A.; Seifitokaldani, A.; Sargent, E. H.; Ajayan, P. M.; Hu, J.; Kibria, M. G. High-Density Cobalt Single-Atom Catalysts for Enhanced Oxygen Evolution Reaction. *J. Am. Chem. Soc.* **2023**. *145*, 8052–8063. DOI:10.1021/jacs.3c00537.

60. Guo, H.; Feng, Q.; Zhu, J.; Xu, J.; Li, Q.; Liu, S.; Xu, K.; Zhang, C.; Liu, T. Cobalt Nanoparticle-Embedded Nitrogen-Doped Carbon/Carbon Nanotube Frameworks Derived from a Metal–Organic Framework for Tri-Functional ORR, OER and HER Electrocatalysis. *J. Mater. Chem. A* **2019**, *7*, 3664–3672. DOI:10.1039/C8TA11400E.

61. Kong, F.; Cui, X.; Huang, Y.; Yao, H.; Chen, Y.; Tian, H.; Meng, G.; Chen, C.; Chang, Z.; Shi, J. N-Doped Carbon Electrocatalyst: Marked ORR Activity in Acidic Media without the Contribution from Metal Sites? *Angew. Chem. Int. Ed.* **2022**, *61*, e202116290. DOI:10.1002/anie.202116290.

62. He, Y.; Shi, Q.; Shan, W.; Li, X.; Kropf, A. J.; Wegener, E. C.; Wright, J.; Karakalos, S.; Su, D.; Cullen, D. A.; Wang, G.; Myers, D. J.; Wu, G. Dynamically Unveiling Metal–Nitrogen Coordination during Thermal Activation to Design High-Efficient Atomically Dispersed CoN4 Active Sites. *Angew. Chem. Int. Ed.* **2021**, *60*, 9516–9526. DOI:10.1002/anie.202017288.

63. Zhang, J.; Xie, Y.; Jiang, Q.; Guo, S.; Huang, J.; Xu, L.; Wang, Y.; Li, G. Facile Synthesis of Cobalt Cluster-CoNx Composites: Synergistic Effect Boosts Electrochemical Oxygen Reduction. *J. Mater. Chem. A* **2022**, *10*, 16920–16927. DOI:10.1039/D2TA04413G.

64. Zhang, M.; Li, H.; Chen, J.; Ma, F.-X.; Zhen, L.; Wen, Z.; Xu, C.-Y. High-Loading Co Single Atoms and Clusters Active Sites toward Enhanced Electrocatalysis of Oxygen

Reduction Reaction for High-Performance Zn–Air Battery. *Adv. Funct. Mater.* **2023**, *33*, 2209726. DOI:10.1002/adfm.202209726.

65. Sun, Y.; Silvioli, L.; Sahraie, N. R.; Ju, W.; Li, J.; Zitolo, A.; Li, S.; Bagger, A.; Arnarson, L.; Wang, X.; Moeller, T.; Bernsmeier, D.; Rossmeisl, J.; Jaouen, F.; Strasser, P. Activity–Selectivity Trends in the Electrochemical Production of Hydrogen Peroxide over Single-Site Metal–Nitrogen–Carbon Catalysts. *J. Am. Chem. Soc.* **2019**, *141*, 12372–12381. DOI:10.1021/jacs.9b05576.

66. Dong, K.; Liang, J.; Ren, Y.; Wang, Y.; Xu, Z.; Yue, L.; Li, T.; Liu, Q.; Luo, Y.; Liu, Y.; Gao, S.; Hamdy, M. S.; Li, Q.; Ma, D.; Sun, X. Electrochemical Two-Electron O_2 Reduction Reaction toward H_2O_2 Production: Using Cobalt Porphyrin Decorated Carbon Nanotubes as a Nanohybrid Catalyst. *J. Mater. Chem. A* **2021**, *9*, 26019–26027. DOI:10.1039/D1TA07989A.

67. Kim, M.; Nam, D.-H.; Park, H.-Y.; Kwon, C.; Eom, K.; Yoo, S.; Jang, J.; Kim, H.-J.; Cho, E.; Kwon, H. Cobalt-Carbon Nanofibers as an Efficient Support-Free Catalyst for Oxygen Reduction Reaction with a Systematic Study of Active Site Formation. *J. Mater. Chem. A* **2015**, *3*, 14284–14290. DOI:10.1039/C5TA02031J.

68. Bisen, O. Y.; Nandan, R.; Raj, G.; Yadav, A. K.; Nanda, K. K. Rational Designing of Co–N–C Electrocatalysts for Comprehensive Elucidation of Intrinsic and Extrinsic Activities in the Oxygen Reduction Reaction. *ACS Appl. Energy Mater.* **2022**, *5*, 14019 − 14034. DOI:10.1021/acsaem.2c02606.

69. Ma, R.; Lin, G.; Zhou, Y.; Liu, Q.; Zhang, T.; Shan, G.; Yang, M.; Wang, J. A Review of Oxygen Reduction Mechanisms for Metal-free Carbon-based Electrocatalysts. *NPG Comput. Mater.* **2019**, *5*, 78. DOI:10.1038/s41524-019-0210-3